Dynamic Mechanical Properties and Modified Johnson-Cook Model Considering Recrystallization Softening for Nickel Based Powder Metallurgy Superalloys

Chen Ling , Xiaoping Ren * , Xuepeng Wang , Yinghao Li , Zhanqiang Liu , Bing Wang , Jinfu Zhao

Posted Date: 7 December 2023

doi: 10.20944/preprints202312.0453.v1

Keywords: dynamic mechanical properties; constitutive model; dynamic recrystallization; powder metallurgy superalloy

Article

Dynamic Mechanical Properties and Modified Johnson-Cook Model Considering Recrystallization Softening for Nickel Based Powder Metallurgy Superalloys

Chen Ling [1,2], Xiaoping Ren [1,2,*], Xuepeng Wang [1,2], Yinghao Li [1,2], Zhanqiang Liu [1,2], Bing Wang [1,2] and Jinfu Zhao [1,2]

[1] School of Mechanical Engineering, Shandong University, China;
[2] Key National Demonstration Center for Experimental Mechanical Engineering Education/Key Laboratory of High Efficiency and Clean Mechanical Manufacture of MQE, China)
* Correspondence: author, Email: renxiaoping@sdu.edu.cn, Postal address: School of Mechanical Engineering, Shandong University, Jingshi Road 17923, Jinan 250061, P. R. China, Telephone: +86-531-88392329.)

Abstract: The material undergoes high temperature and high strain rate deformation process during cutting process, may induce the dynamic recrystallization behavior and result the evolution of dynamic mechanical properties of the material to be machined. In this paper, the modified Johnson-Cook(J-C) model for Nickel based powder metallurgy superalloy considering dynamic recrystallization behavior in high strain rate and temperature is proposed. The dynamic mechanical properties of the material under different strain rates and temperature conditions are obtained by quasi-static compression test and split Hopkinson pressure bar (SHPB) test. The coefficients of the modified J-C model are obtained by linear regression method. The modified model is verified by comparison with experimental and model prediction results. The results show that the modified J-C model proposed in this paper can accurately describe the mechanical properties of nickel-based powder metallurgy superalloys at high temperature and high strain rate. Which provides help for studying the cutting mechanism and finite element simulation of nickel-based powder metallurgy superalloy.

Keywords: dynamic mechanical properties; constitutive model; dynamic recrystallization; powder metallurgy superalloy

1. Introduction

Comparing with cast and wrought superalloy, the powder metallurgy (PM) superalloy has widely used in advanced aero-engine turbine disks [1,2] due to its homogeneous microstructure, fine grains, higher yield strength and no mace segregation [3,4], etc. Although PM is a near-forming process, machining is still a necessary process to meet the final accuracy requirements. However, because of low thermal conductivity and low elastic modulus, PM superalloy are deemed too difficult to machining materials [5,6].

The external power is converted into deformation energy in the cutting process. At the same time, the heat is not easy to release, causing the tool and workpiece material temperature rise, resulting in material softening [7]. On the other hand, with the increase of strain, the material work hardening occurs. The interaction between the two makes the material strength not only a function of strain, but also a function of strain rate and deformation temperature, which is called the constitutive relation equation [8,9]. Establishing the accurate constitutive relationship of the workpiece material in the cutting deformation zone is the key to study the cutting deformation mechanism.

The constitutive equation for the cutting process is mainly divided into two categories, namely phenomenological models and physical models [10]. Compared with physical models, phenomenological models have become the widely used one due to its simple form and wide applicability [11]. As the most widely used phenomenological model, the Johnson-Cook (J-C) model

 doi:10.20944/preprints202312.0453.v1

[12] is given in the form of three-part product, representing strain hardening, strain rate hardening and thermal softening, respectively. However, the above three items of the J-C model are considered to be independent of each other, and the effects of the microstructure of the material itself and the adiabatic temperature rise on the flow stress are not considered [13–15].

The occurrence of dynamic recrystallization in the cutting process has been confirmed by researchers [16,17]. Dynamic recrystallization not only refines the grain size of the workpiece material, but also produces a softening phenomenon that cannot be ignored in the flow stress of the material during the deformation process.

A constitutive equation that can accurately describe the microscopic deformation process is still to be realized. Calamaz M et al. [18] established a JC-TANH modified model to describe the phenomenon of soft flow caused by dynamic recrystallization of cutting titanium alloy materials, and applied it to the finite element software. This model was verified by Ulutan [18] in software *Deform*. Other similar corrections to the J-C constitutive equation can be found in the literature [19,20].

However, the above modified models only use the temperature ($T_m/2$) condition as the critical condition for recrystallization. According to the modified J-C model of DENGUIR et al. [21], the recrystallization strain threshold was proposed. This critical condition takes into account the combined effects of temperature and strain rate.

The cutting process is a strong coupling process of transient high strain, high strain rate and temperature. The occurrence of recrystallization is very important to the dynamic mechanical properties of PM superalloy. However, the current research on the modified constitutive equation considering recrystallization for difficult-to-machine materials focuses on titanium alloys. The research on the dynamic mechanical properties of PM superalloy at high temperature and high strain rate, especially the influence of dynamic recrystallization, is still very scarce.

In this paper, the dynamic mechanical properties of powder metallurgy superalloy were analyzed by quasi-static test and SHPB test. A modified constitutive model considering the dynamic recrystallization behavior of the cutting process is established. The parameters of the modified model are obtained by linear fitting of the experimental data. Finally, it is verified that the model has good accuracy.

2. Experimentals

2.1. Specimen preparation

The FGH96 superalloy used in this study is prepared by hot isostatic pressing (HIP) and its composition is shown in Table 1. The experiment method is consisted with two parts, which are quasi-static state compression tests and SHPB tests.

Table 1. Chemical composition of FGH96 superalloy.

Element	C	Al	Ti	Cr	Co	Nb	Mo	W	Ni
Wt. (%)	0.03	2.2	3.7	16	13	0.8	4	4	Bal

The samples sizes for quasi-static state compression tests and SHPB tests are $\phi 3mm \times 3mm$ and $\phi 2mm \times 2mm$, respectively. By grinding the end face and outer surface of the sample obtained by wire cutting, the sample has higher dimensional accuracy and lower surface roughness ($R_a \leq 0.8mm$). In addition, it is necessary to ensure that the parallelism of the two ends is less than 0.01 mm, so as to reduce the experimental error caused by the sample.

2.2. Quasi-static state compression tests

The quasi-static compression test of FGH96 superalloy is carried out in the electric universal testing machine. All the experiments are carried out at room temperature. The strain rate is set at $0.001s^{-1}$ by controlling the loading speed ($0.2mm/min$). The force and displacement in the experiment are output by the control software, and then processed by Origin software to obtain the stress-strain

Preprints (www.preprints.org) | NOT PEER-REVIEWED | Posted: 7 December 2023 doi:10.20944/preprints202312.0453.v1

curve. In order to ensure the reliability of the data, three repeated tests were carried out for each specimen, and the average value was obtained.

2.3. SHPB tests

The SHPB equipment system are schematically illustrated in Figure 1. In order to obtain higher strain rate, the diameter of the incident bar and the transmitted bar is reduced to 5*mm*.

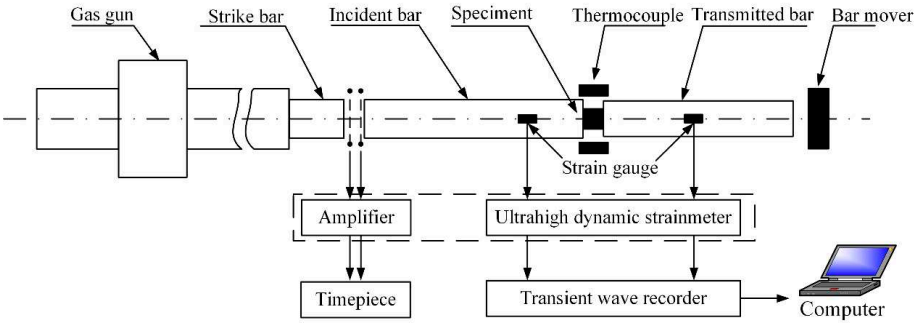

Figure 1. Schematic diagram of SHPB equipment system.

The strains of sample could be recorded by strain gauges, which are attachment on the incident bar and transmitted bar. According to the one-dimensional stress wave theory, the engineering strain ε_{eng}, engineering stress σ_{eng} and strain rate $\dot{\varepsilon}_{eng}$ sample can be calculated by Equation (1)-(3). The temperature is controlled by resistance-heated furnace. To ensure the accuracy of the data, three experiments are repeated for each sample.

$$\varepsilon_{eng}(t) = -\frac{2c_0}{l_0}\int_0^t \varepsilon_r(t)dt \tag{1}$$

$$\sigma_{eng} = \frac{AE\varepsilon_t}{A_0} \tag{2}$$

$$\dot{\varepsilon}_{eng} = -\frac{2c_0\varepsilon_r}{l_0} \tag{3}$$

Where, c_0 is the wave speed in the incident bar, E and A are the Young's modulus and the cross-sectional area of the bars. A_0 and l_0 are the cross-sectional area and the length of the cylindrical specimen. ε_r and ε_t are the reflected and transmitted strains, respectively, when the reflected and transmitted waves propagate independently.

Under the condition that the material is incompressible, the true strain ε_T, true stress σ_T and true strain rate $\dot{\varepsilon}_T$ of the specimen can be obtained, by Equation(4)-(6).

$$\varepsilon_T(t) = -\ln(1-\varepsilon_{eng}) \tag{4}$$

$$\sigma_T = \sigma_{eng}(1-\varepsilon_{eng}) \tag{5}$$

$$\dot{\varepsilon}_T = \frac{d\varepsilon_T}{dt} \tag{6}$$

The experimental conditions of SHPB tests are shown in Table 2.

 doi:10.20944/preprints202312.0453.v1

Table 2. Experimental conditions of SHPB tests.

Variable	Values
Strain rate $\dot{\varepsilon}$ (s^{-1})	4000, 6000, 10000, 12000
Temperature T (℃)	25, 200, 400, 600, 700, 800

3. Modified constitutive model

The modified model proposed in this paper considers the coupling effect of strain, strain rate and temperature and the influence of microstructure transformation on the basis of JC model, as shown in Equation (7).

$$\sigma = (A + B\varepsilon^n)(1 + C\ln\frac{\dot{\varepsilon}}{\dot{\varepsilon}_0})\left[1 - \left(\frac{T - T_0}{T_m - T_0}\right)^m\right]H(\varepsilon, \dot{\varepsilon}, T) \tag{7}$$

Where, A represents the yield stress, B and n represent the material strain hardening coefficients, ε represents the true strain, C represents the viscosity coefficient, $\dot{\varepsilon}$ represents the strain rate, ε_0 represents the reference strain rate, T represents the temperature, T_m represents the material melting temperature, T_0 represents the room temperature, and m represents the thermal softening coefficient. The effect of dynamic recrystallization on flow stress is characterized by adding a correction item $H(\varepsilon, \dot{\varepsilon}, T)$ to J-C model. The mathematical expressions of $H(\varepsilon, \dot{\varepsilon}, T)$ are shown in Equation (8)-(10). Considering that the recrystallization threshold is affected by both temperature and strain rate, it is expressed by Equation (11).

$$H(\varepsilon, \dot{\varepsilon}, T) = \frac{1}{1 - h(\varepsilon, \dot{\varepsilon}) \cdot u(\dot{\varepsilon}, T)} \tag{8}$$

$$u(\dot{\varepsilon}, T) = \begin{cases} 0, \varepsilon < \varepsilon_r \\ 1, \varepsilon \geq \varepsilon_r \end{cases} \tag{9}$$

$$h(\varepsilon, \dot{\varepsilon}) = \frac{h_0}{\varepsilon} + h_1 - (\frac{h_0}{\varepsilon} + h_2)\ln\left(\frac{\dot{\varepsilon}}{\dot{\varepsilon}_0}\right) \tag{10}$$

$$\varepsilon_r = r_0 + r_1 T^{r_2} + r_3 \dot{\varepsilon}^{r_4} + r_5 T^{r_2} \dot{\varepsilon}^{r_4} \tag{11}$$

Where, h_i (i=0,1,2) and r_i (i =0, 1…5) are material constants, ε_r is the critical strain for the occurrence of dynamic recrystallization, which is expressed by Equation (11).

4. Results and discussion

4.1. Dynamic mechanical properties

4.1.1. Characteristics of stress-strain curve

The stress-strain curve of FGH96 superalloy obtained by quasi-static compression test is shown in Figure 2. According to Figure 2, in the first stage of compression process (*OA*), the material undergoes elastic deformation with the stress increases linearly with the increase of strain. When the strain reaches point A, the growth rate of stress slows down with the increase of strain, indicating that the material enters the plastic deformation stage (*AB*), showing obvious work hardening phenomenon. When the strain exceeds the strain at point *B*, the material enters the damage deformation stage which is marked by the decrease of stress with the increase of strain.

According to the above analysis, there is no obvious yield phenomenon in the quasi-static compression process of FGH96 superalloy. The yield stress of bulk samples was measured by 0.2%

Preprints (www.preprints.org) | NOT PEER-REVIEWED | Posted: 7 December 2023 doi:10.20944/preprints202312.0453.v1

strain shift method, that is, the stress value when 0.2% plastic deformation occurs is taken as its yield strength (point *A* in Figure 2). The yield strength of FGH96 superalloy is $\sigma_{0.2}$=773 *MPa*.

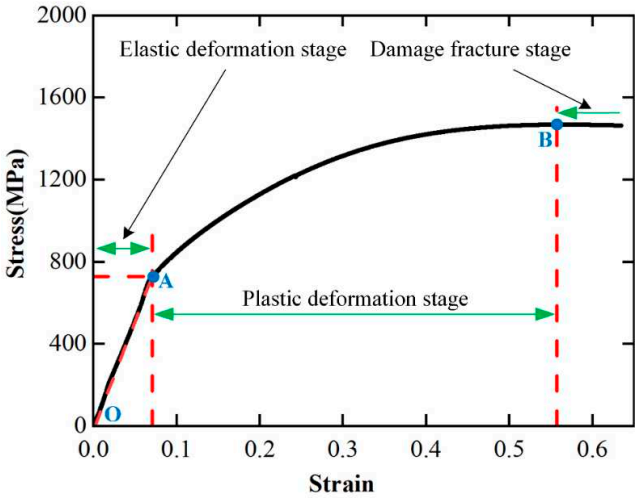

Figure 2. Stress-strain curve of FGH96 superalloy in the quasi-static compression test.

The effect of strain rate on the stress-strain curve of FGH96 superalloy obtained by SHPB tests at different temperatures (25℃, 200℃, 400℃, 600℃, 700℃, 800℃) is shown in Figure 3. According to Figure 3a, when the temperature is 25℃, the maximum strains in the plastic deformation stage corresponding to the strain rates of 4000s^{-1},6000s^{-1},10000s^{-1} and 12000s^{-1} are 0.3, 0.4, 0.6 and 0.7, respectively. That is to say, the plastic deformation stage at room temperature increases significantly with the increase of strain rate, and the increase is as high as 200 %. According to Figure 3b–f, under high temperature deformation conditions (200℃, 400℃, 600℃, 700℃, 800℃), compared with the lower strain rate level, the plastic deformation stage of the material under high strain rate conditions also increases significantly. In summary, the PM superalloy has obvious plasticizing effect in the deformation process over a wide range of strain rate.

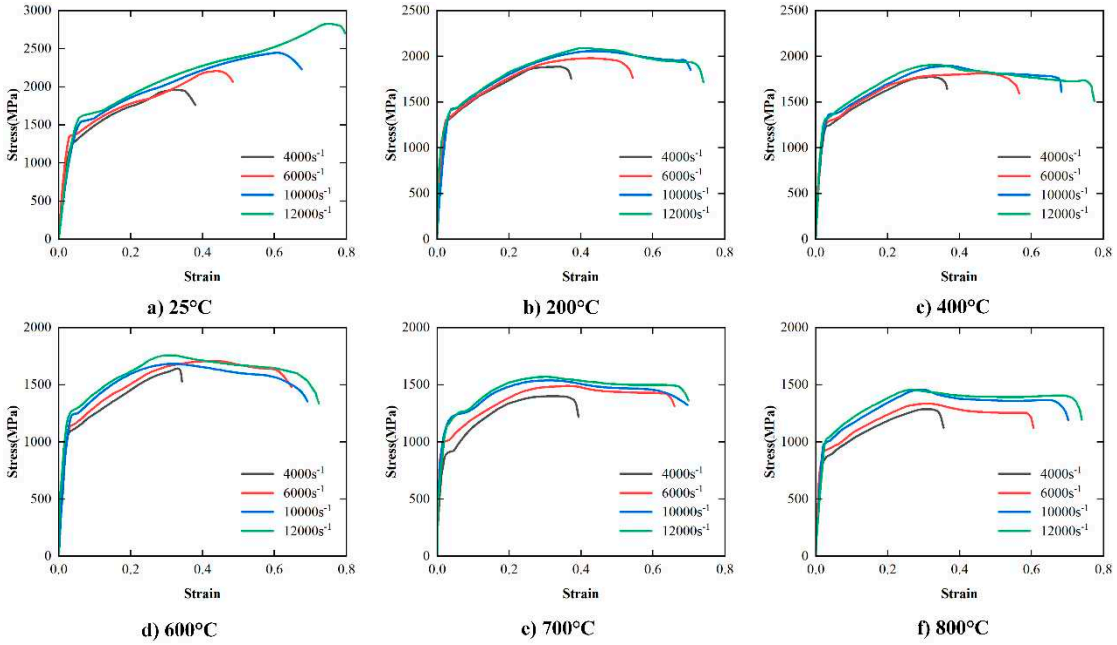

Figure 3. Stress-strain curves of FGH96 superalloy over the wide range of temperature in the SHPB tests. a)25℃; b)200℃; c)400℃; d)600℃; e)700℃; f)800℃.

Preprints (www.preprints.org) | NOT PEER-REVIEWED | Posted: 7 December 2023 doi:10.20944/preprints202312.0453.v1

The effect of temperature on the stress-strain curve of FGH96 superalloy at different strain rates ($4000s^{-1}$, $6000s^{-1}$, $10000s^{-1}$, $12000s^{-1}$) is shown in Figure 4. According to Figure 4a–d, at the same strain rate, the stress in the plastic deformation stage decreases with the increase of temperature, showing obvious temperature softening effect.

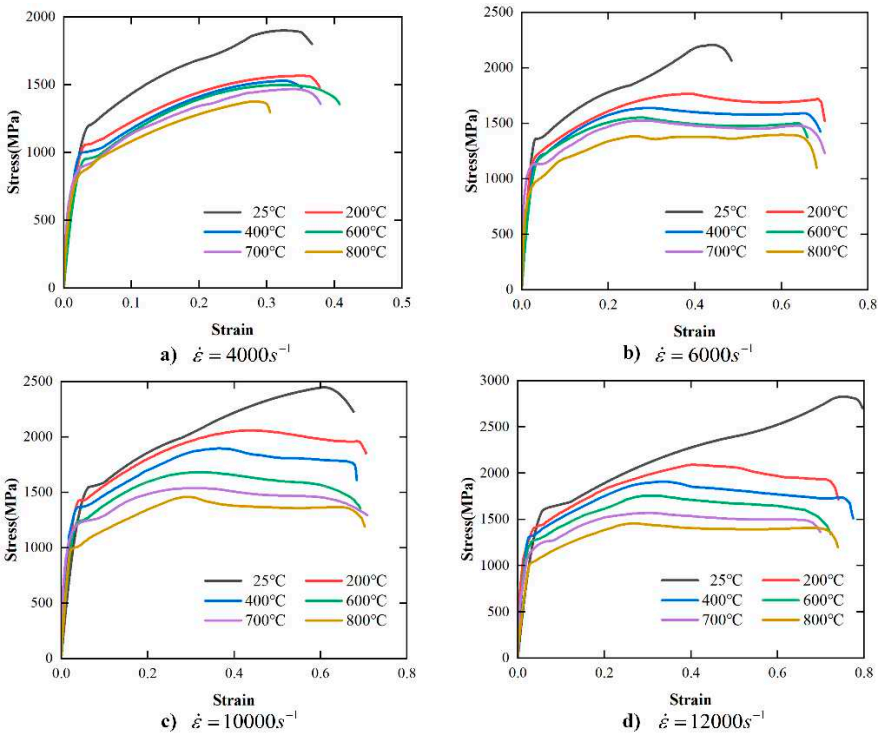

Figure 4. Stress-strain curves of FGH96 superalloy over the wide range of strain rate in the SHPB tests. a) $4000s^{-1}$; b) $6000s^{-1}$; c) $10000s^{-1}$; d) $12000s^{-1}$.

Table 3 shows the yield stress at different temperatures and strain rates under SPHB test conditions. Compared with the yield stress (*773MPa*) obtained by quasi-static compression test at room temperature, the yield stress obtained by SPHB tests at high temperature and high strain rate increases significantly. When the strain rate is $12000s^{-1}$, the yield strength reaches *1616MPa*. According to Table 3, when the temperature is 200 ℃, 400 ℃, 600 ℃, 700 ℃ and 800 ℃, the yield strength increases with the increase of strain rate. It is worth noting that the flow stress of the material also increases with the increase of strain rate (Figure 3), which indicates that the PM superalloy material exhibits a significant strain rate hardening effect.

In addition, under the same strain rate loading conditions, the yield strength of the PM superalloy decreases with the increase of temperature. Combined with Figure 4, the flow stress and yield strength decrease with the increase of temperature, which further confirms the temperature softening effect of the PM superalloy.

Table 3. Yield strength at different temperatures and strain rates (*MPa*).

Strain rate (s^{-1})	**Temperature, *T* (℃)**					
	25	**200**	**400**	**600**	**700**	**800**
4000	1315	1305	1234	1097	903	883
6000	1359	1318	1280	1142	1001	926
10000	1544	1544	1322	1227	1182	994
12000	1616	1616	1355	1271	1205	1043

Preprints (www.preprints.org) | NOT PEER-REVIEWED | Posted: 7 December 2023 doi:10.20944/preprints202312.0453.v1

4.1.2. Strain-hardening

In order to quantitatively analyze the strain hardening phenomenon of PM superalloy, the strain hardening rate Q is calculated by Equation (12).

$$Q_i = \frac{\partial \sigma}{\partial \varepsilon} = \frac{\sigma_i - \sigma_{i-1}}{\varepsilon_i - \varepsilon_{i-1}} \tag{12}$$

Where, ε_i and σ_i represent the strain and the stress of the ith experiment, respectively. ε_{i-1} and σ_{i-1} represent the strain and the stress of the (i-1)th experiment.

Based on the quasi-static compression experimental data, the strain hardening rate-strain curve of the PM superalloy obtained according to the Equation (12) is shown in Figure 5. According to Figure 5, in the elastic deformation stage, the strain hardening rate Q of the material decreases sharply with the increase of strain. In the plastic deformation stage (AB), the decrease rate of strain hardening rate slows down, and at point B, it decreases to 0 (it is no longer in the hardening state). In the damage deformation stage, the strain hardening rate is less than 0, and the material is damaged and deformed. Therefore, it can be concluded that during the quasi-static compression test, the strain hardening phenomenon of FGH96 superalloy is significant, and with the continuous increase of strain, the strain hardening effect gradually weakens, and reaches equilibrium at point B. This is because in the process of quasi-static compression deformation, with the increase of strain, thermal softening occurs inside the material[22].

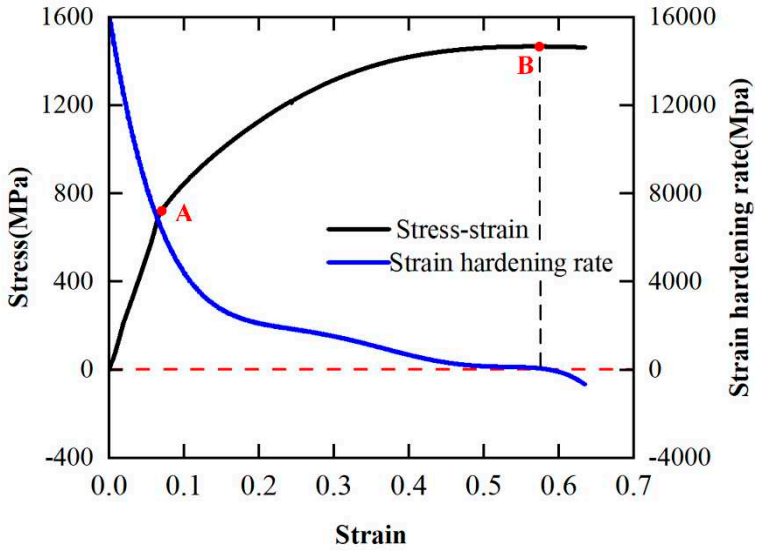

Figure 5. Strain hardening rate-strain curve under quasi-static compression test conditions.

When the temperature is 700°C, the strain hardening rate-strain curve of the PM superalloy at different strain rates is shown in Figure 6. According to Figure 6, the PM superalloy still exhibits obvious strain hardening under high temperature and high strain rate conditions. However, it is worth noting that in the plastic deformation stage, the strain hardening rate Q of the material at strain rate of 4000s^{-1} always remains positive. In contrast, the Q of the material at the strain rate of 6000s^{-1} continues to decrease and reaches a negative state after reaching zero. This is because the material not only has the thermal softening effect, but also superimposes the recrystallization softening effect, so that the hardening effect in the plastic deformation stage is greatly weakened, and the flow softening phenomenon appears [23].

Preprints (www.preprints.org) | NOT PEER-REVIEWED | Posted: 7 December 2023 doi:10.20944/preprints202312.0453.v1

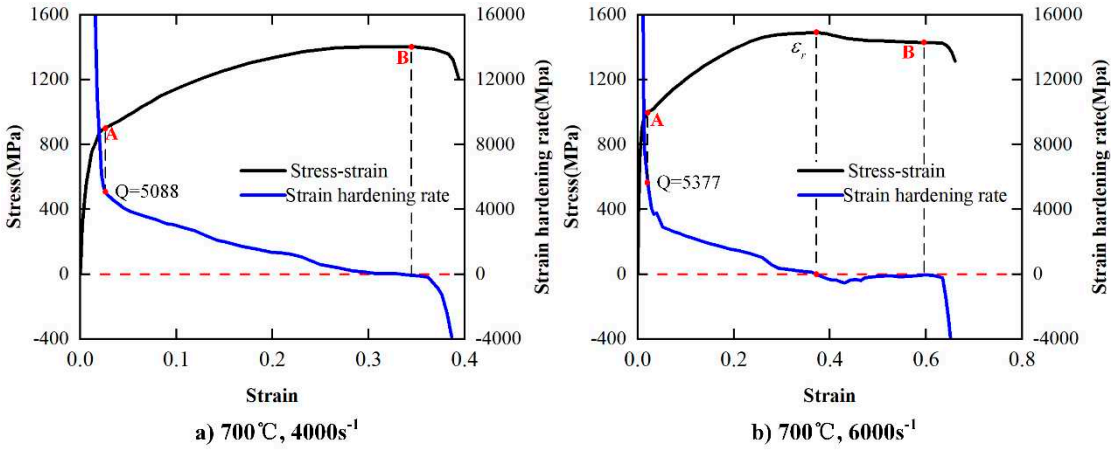

Figure 6. The strain hardening rate-strain curve at 700℃ obtained by SHPB tests. a) 4000s^{-1}; b) 6000s^{-1}.

4.1.3. Adiabatic induced increase of temperature

According to Section 4.1.1, the PM superalloy has obvious plasticizing effect during high temperature and high strain rate deformation. Researchers have found that the adiabatic temperature rise during material deformation is one of the important factors that cannot be ignored in the plasticizing effect [24]. In addition, the adiabatic temperature rise makes the actual temperature inside the material higher than the experimental loading temperature, which reduces the dislocation slip resistance and strengthens the internal softening of the material. Under the experimental conditions in this paper, the adiabatic temperature rise ΔT in the process of material deformation can be obtained by Equation (13).

$$\Delta T = \frac{\eta}{\rho C_p}\int_0^{\varepsilon}\sigma d\varepsilon \tag{13}$$

Where, η is the plastic work-heat conversion coefficient, for the experimental deformation conditions in this paper, it take 0.9[25]; ρ is the material density; C_p is the specific heat capacity at atmospheric pressure. The specific heat capacity C_p of the PM superalloy FGH96 superalloy at different temperatures is shown in Table 4.

Table 4. Specific heat capacity of FGH96 superalloy at different temperatures.

Temperature, T (℃)	**25**	**200**	**400**	**600**	**700**	**800**
C_p (kJ/ (kg·K))	0.391	0.422	0.455	0.487	0.503	0.525

Figure 7 shows the influence of loading temperature on adiabatic temperature rise of FGH96 superalloy under different strain rates. According to Figure 7, at the same strain rate, the adiabatic temperature rise decreases with the increase of temperature. For example, at the strain rate of 12000s^{-1}, as the loading temperature increases from 25 ℃ to 800 ℃, the adiabatic temperature rise decreases from 100 ℃ to 30℃ (reduced by 70%). At the same time, when the strain rate is 4000s^{-1}, the adiabatic temperature rise decreases from 35 ℃ to 15 ℃ with the increase of loading temperature (reduced by 60%). It can be seen that with the decrease of strain rate, the rate of adiabatic temperature rise decreasing with the increase of loading temperature is obviously reduced. From the above, with the decrease of strain rate, the reduction rate of adiabatic temperature rise decreases significantly with the increase of loading temperature. At the same loading temperature, the higher the strain rate, the higher the adiabatic temperature rise. For example, at 200 ℃, the corresponding adiabatic temperature rise at strain rates of 4000 s^{-1}, 6000 s^{-1}, 10000 s^{-1} and 12000 s^{-1} are 30 ℃, 40 ℃, 65 ℃ and 70 ℃, respectively.

Preprints (www.preprints.org) | NOT PEER-REVIEWED | Posted: 7 December 2023 doi:10.20944/preprints202312.0453.v1

At the same time, compared with the temperature of 25 ℃, 200 ℃ and 400 ℃, the adiabatic temperature rises at 600 ℃, 700 ℃ and 800 ℃ decreases significantly with the increase of strain rate.

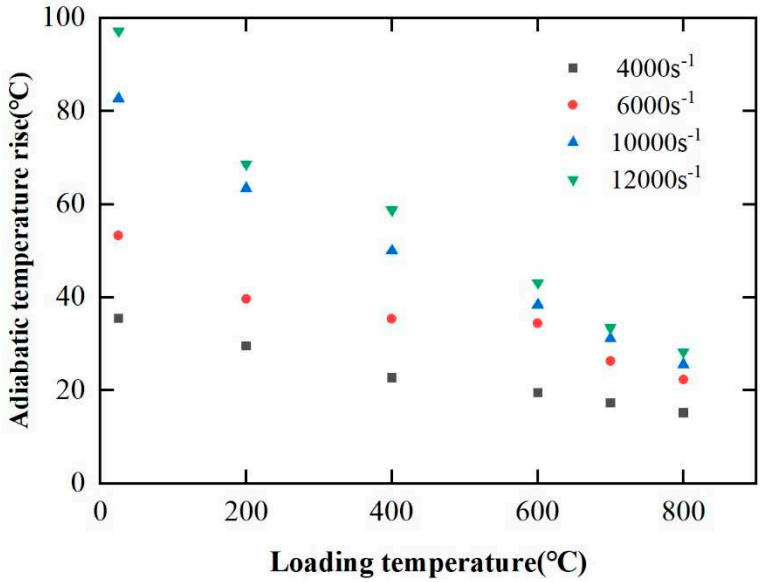

Figure 7. The influence of loading temperature on adiabatic temperature rise during deformation under different strain rates.

4.1.4. The strain rate sensitivity

According to Section 4.1.1, FGH96 superalloy exhibits strain rate strengthening effect in the plastic deformation stage. In order to describe the degree of strain rate strengthening of the material, the strain rate sensitivity coefficient q is introduced, as shown in Equation (14). The larger the strain rate sensitivity coefficient q, the stronger the strain rate sensitivity of the material.

$$q = \frac{\partial \ln \sigma}{\partial \ln \dot{\varepsilon}} \tag{14}$$

Figure 8 shows the influence of strain on the strain rate sensitivity coefficient of FGH96 superalloy at different temperatures. According to Figure 8, the strain rate sensitivity coefficient decreases with the increase of strain under the experimental temperature conditions. For example, when the temperature is 600 ℃, the strain rate sensitivity coefficient decreases from 0.11 to 0.09 with the increase of strain (from 0.1 to 0.4). It is worth noting that the influence of temperature on the strain rate sensitivity coefficient is not obvious. For example, for the temperature conditions of 200 ℃ and 400 ℃, the strain rate sensitivity coefficient is lower than the strain rate sensitivity coefficient of 25 ℃. However, when the temperature is greater than 600 ℃, the strain rate sensitivity coefficient becomes larger and increases with the increase of temperature. At the same time, when the temperature is 800 ℃ and the strain is 0.1, the biggest strain rate sensitivity coefficient is 0.155 (less than 0.2), which shows that FGH96 superalloy exhibits weak strain rate sensitivity.

Preprints (www.preprints.org) | NOT PEER-REVIEWED | Posted: 7 December 2023 doi:10.20944/preprints202312.0453.v1

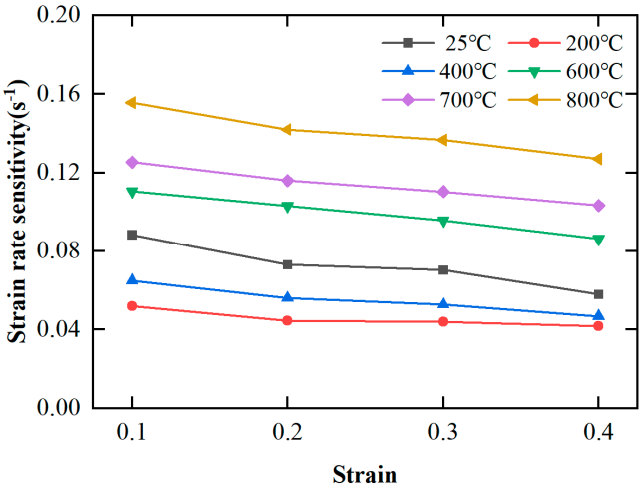

Figure 8. Strain rate sensitivity coefficient-strain curves of FGH96 superalloy at different temperatures.

4.1.5. The temperature sensitivity

According to section 4.1.1, FGH96 superalloy shows a strong temperature softening effect in the plastic deformation stage. In order to quantitatively describe the temperature sensitivity of the material, the temperature sensitivity coefficient s is introduced, as shown in Equation (15). The greater the temperature sensitivity coefficient s, the stronger the temperature sensitivity of the material.

$$s = \left| \frac{\partial \ln \sigma}{\partial \ln T} \right|_{\varepsilon,\dot{\varepsilon}} \tag{15}$$

The variation of the temperature sensitivity coefficient of FGH96 superalloy with temperature at different strain rates calculated by Equation (15) is shown in Figure 9. According to Figure 9, the temperature sensitivity coefficient increases significantly with the increase of temperature under the same strain rate. When the strain rate is 4000s^{-1}, the temperature sensitivity coefficient is 0.1 at 200 ℃, and reaches 1.2 at 800℃, which is increased by 1100%. At the same time, the temperature sensitivity coefficient decreases with the increase of strain rate. When the temperature is 800 ℃, the temperature sensitivity coefficient is 1.3 at 4000s^{-1}, and decreases to 0.9 at 12000^{-1}, with a decrease of 30%. From the above, the temperature sensitivity of the PM superalloy increases significantly with the increase of temperature and decreases with the decrease of strain rate. In summary, FGH96 superalloy exhibits strong temperature sensitivity.

Preprints (www.preprints.org) | NOT PEER-REVIEWED | Posted: 7 December 2023 doi:10.20944/preprints202312.0453.v1

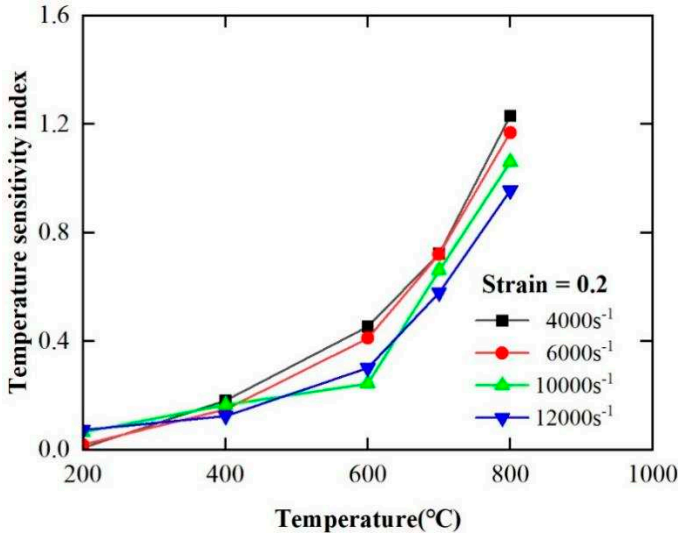

Figure 9. Temperature sensitivity coefficient-temperature curves of FGH96 superalloy at different strain rate.

4.2. Construction of constitutive model

4.2.1. Recrystallization critical condition

The effect of dynamic recrystallization on the stress-strain curve of the material is shown in Figure 10. If there is no dynamic recrystallization during the deformation process, the flow stress of the material increases slowly with the increase of strain, as shown in the black solid line in Figure 10. When the strain reaches the critical strain of dynamic recrystallization, the flow stress decreases, which is manifested as the recrystallization softening effect as shown in the red line in Figure 10. However, when the strain reaches a certain value (critical strain ε_r), the material undergoes dynamic recrystallization. At this time, the flow stress shows a significant downward trend, as shown in the red solid line in Figure 10, which is the flow softening phenomenon. Therefore, the determination of the critical condition of dynamic recrystallization, that is, the critical strain, is the key to the study of dynamic recrystallization flow softening.

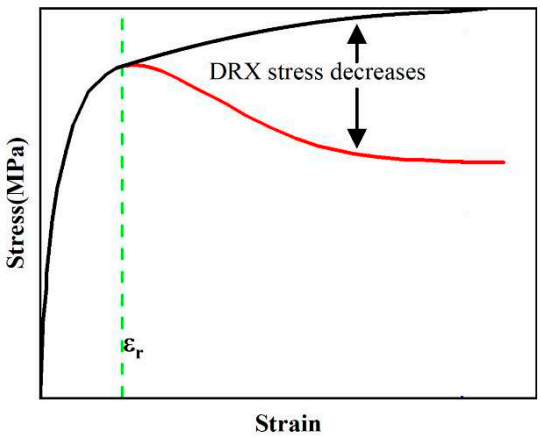

Figure 10. Flow softening of stress-strain curve induced by dynamic recrystallization.

The dynamic recrystallization critical strain of the PM superalloy obtained under the experimental conditions in this paper is shown in Table 5. It can be seen from the data in Table 5 that the critical strain of dynamic recrystallization of PM superalloy is not only related to the deformation temperature, but also related to the strain rate, which verifies the conclusion of Denguir [21]. The

Preprints (www.preprints.org) | NOT PEER-REVIEWED | Posted: 7 December 2023 doi:10.20944/preprints202312.0453.v1

critical strain decreases with the increase of temperature and decreases with the increase of strain rate.

Table 5. Critical strain ε_r under different temperature and strain rate conditions.

strain rate (s^{-1})	Temperature, T (℃)				
	200	400	600	700	800
6000			0.4233	0.3621	0.3211
10000	0.4033	0.3640	0.3199	0.3144	0.2911
12000	0.3999	0.3443	0.3091	0.3051	0.2698

Based on the data in Table 3, the fitting surface of the critical strain is obtained by polynomial fitting (Equation (11)), is shown in Figure 11.

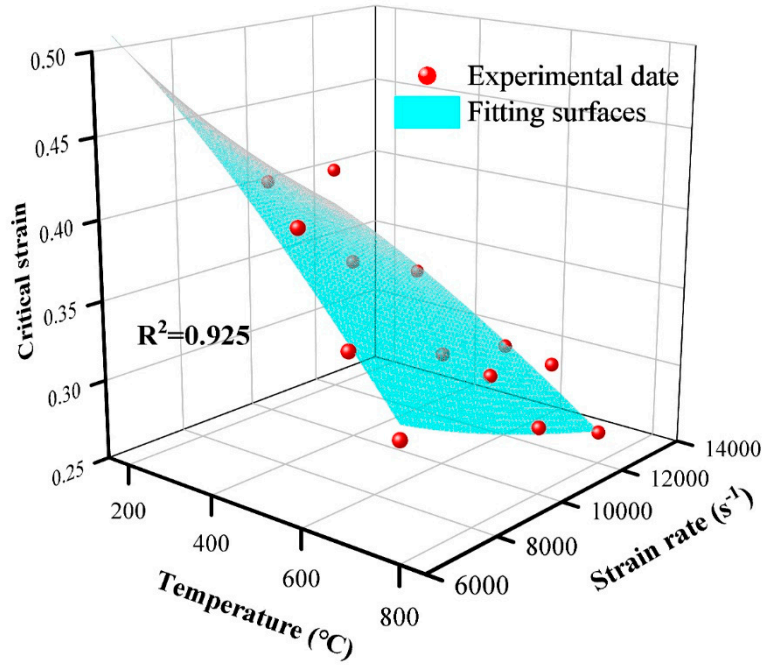

Figure 11. Solving method and results of dynamic recrystallization critical strain.

The equation of calculating the critical strain of dynamic recrystallization of PM superalloy under experimental conditions in this paper is shown in Equation (16).

$$\varepsilon_r = 1.445 - 5.85\times10^{-5}T^{1.415} - 0.139\dot{\varepsilon}^{0.215} + 6.45\times10^{-6}T^{1.415}\dot{\varepsilon}^{0.215} \quad (16)$$

4.2.2. Identification of constitutive model's coefficients

(1) Linear regression method

The modified J-C constitutive model (Equation (7)) represents strain hardening effect, strain rate strengthening effect, thermal softening effect and recrystallization softening effect from left to right. According to the linear regression parameter solving method, A, B, C, n, m and H_i are the parameters to be fitted, $\dot{\varepsilon}_0$, T_0 and T_m are 0.001s^{-1}, 25°C and 1350°C, respectively.

The strain hardening coefficient can be obtained by processing the quasi-static compression test data at room temperature. The proposed constitutive model is simplified as shown in Equation (17).

Preprints (www.preprints.org) | NOT PEER-REVIEWED | Posted: 7 December 2023 doi:10.20944/preprints202312.0453.v1

The quasi-static compression tests permitted to determine the yield stress, which is represented by the coefficient A (Figure 12a). The Equation (18) was obtained by taking the logarithm on both sides of the Equation (17). The solution of the coefficients n and B can be obtained by a slope and an intercept of fitting straight line (Figure 12b). As shown in Figure 12, $A = \sigma_{0.2} = 773MPa$, n = 0.667, B = 1271MPa.

$$\sigma = A + B\varepsilon^{n} \tag{17}$$

$$\ln(\sigma - A) = n\ln\varepsilon + \ln B \tag{18}$$

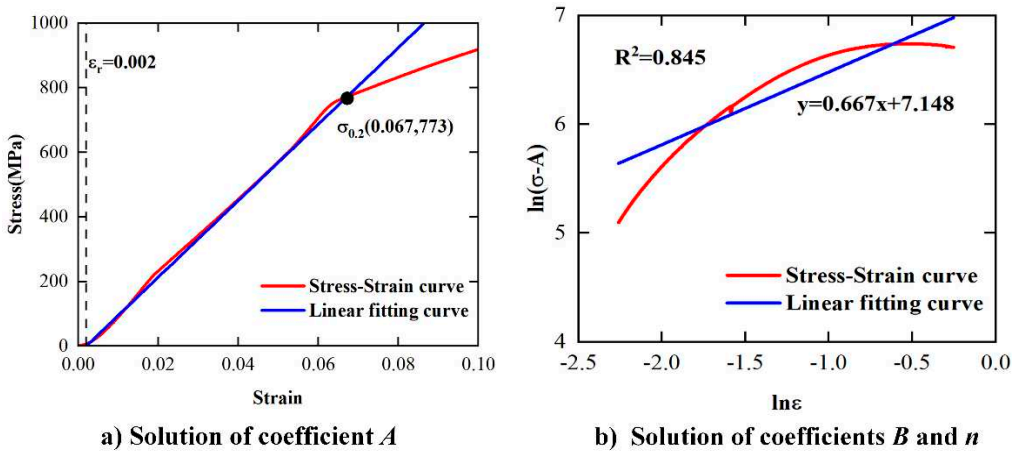

Figure 12. Solution of coefficients A, B and n. a) Solution of coefficient A; b) Solution of coefficients B and n.

The strain rate sensitivity coefficient C, the thermal softening index m and the recrystallization softening correction coefficient H_i in the modified J-C constitutive model were obtained from the result of SHPB experiments.

According to SHPB tests at room temperature for different strain-rates, the constitutive equation simplified to Equation (19). The stress-strain curves of PM materials at different strain rates at room temperature in this paper are shown in Figure 13.

$$\sigma = (A + B\varepsilon^{n}) \cdot (1 + C\ln\frac{\dot{\varepsilon}}{\dot{\varepsilon}_0}) \tag{19}$$

Preprints (www.preprints.org) | NOT PEER-REVIEWED | Posted: 7 December 2023 doi:10.20944/preprints202312.0453.v1

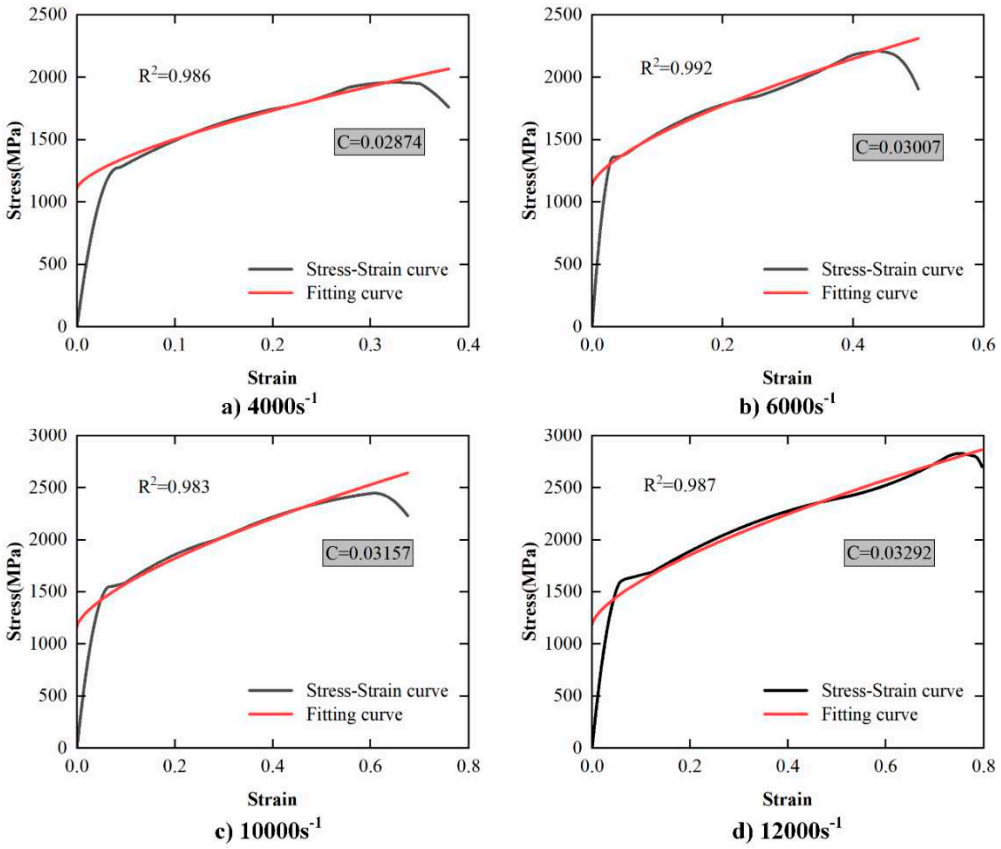

Figure 13. The results of strain rate sensitivity coefficient *C*. a) 4000s^{-1}; b)6000s^{-1}; c)10000s^{-1}; d)12000s^{-1}.

The thermal softening coefficient m is determined according to Equation (20). The data of the SHPB tests under high temperature conditions were used. Finally, the fitting relationship between m and strain-rate is obtained as shown in Figure 14.

$$m\ln\left(\frac{T-T_0}{T_m-T_0}\right)=\ln\left(1-\frac{\sigma}{\left(A+B\cdot\varepsilon^n\right)\cdot\left(1+C\cdot\ln\frac{\dot{\varepsilon}}{\dot{\varepsilon}_0}\right)}\right) \tag{20}$$

Preprints (www.preprints.org) | NOT PEER-REVIEWED | Posted: 7 December 2023 doi:10.20944/preprints202312.0453.v1

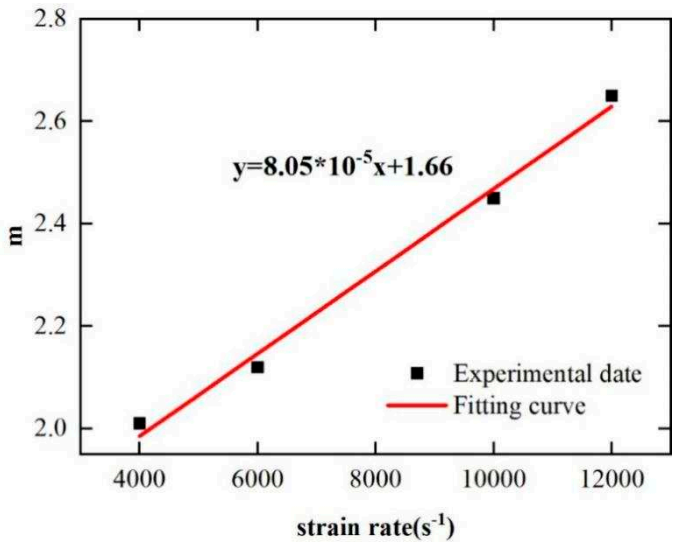

Figure 14. Solution of thermal softening coefficient *m*.

The coefficients h_i (i=0, 1, 2) related to the dynamic recrystallization can be obtained according to Equation (21).

$$\frac{\sigma}{f(\varepsilon)f(\dot{\varepsilon})f(T)}=\frac{1}{1-(\frac{h_0}{\varepsilon}+h_1)+(\frac{h_0}{\varepsilon}+h_2)\ln(\frac{\dot{\varepsilon}}{\dot{\varepsilon}_0})} \tag{21}$$

In summary, the modified constitutive model obtained by the linear regression method is shown in Table 6.

Table 6. Constitutive model coefficients of linear regression method.

Coefficients	Value
A (MPa)	773
B (MPa)	1271
C	0.031
n	0.667
m	$8.05\times10^{-5}\dot{\varepsilon}+1.66$
h_0	-0.015
h_1	-0.015
h_2	0.046
ε_r	$1.445-5.85\times10^{-5}T^{1.415}-0.139\dot{\varepsilon}^{0.215}+6.45\times10^{-6}T^{1.415}\dot{\varepsilon}^{0.215}$

(2) Function iteration method

According to Function iteration method [26,27], the proposed model is shown in Equation (22). The iterative function method determines the coefficients of the prediction model by continuously iterating the function through the optimization algorithm.

$$\sigma=f(\varepsilon)\cdot f(\dot{\varepsilon})\cdot f(T)\cdot f(H_i) \tag{22}$$

The stress values corresponding to the room temperature T_0 and the reference strain rate $\dot{\varepsilon}_0$ conditions are selected as the initial values. The quasi-static compression test data at room

Preprints (www.preprints.org) | NOT PEER-REVIEWED | Posted: 7 December 2023 doi:10.20944/preprints202312.0453.v1

temperature are selected for polynomial fitting to obtain the results of $f(\varepsilon)$, which are shown in Figure 15a. Then, according to the relationship between measured stress in SHPB experiment at room temperature and $f(\varepsilon)$, the relationship between stress and strain rate is obtained by iteration, which is $f(\dot{\varepsilon})$, which are shown in Figure15b. Finally, the results of $f(T)$ and $f(H_i)$ can be obtained according to the high temperature SHPB experimental data by iteration process, as shown in Figure 15c,d, respectively.

In the iterative process, the error R^2 is used to judge the accuracy of the results. When the result meet Equation (23), the result is considered to be accepted.

$$\left|R_k^2 - R_{k-1}^2\right| \le 10^{-3} \tag{23}$$

Where, R_k^2 is the error of determination of the ith iterated function, R_{k-1}^2 is the error of determination of the (i-1)th iterated function.

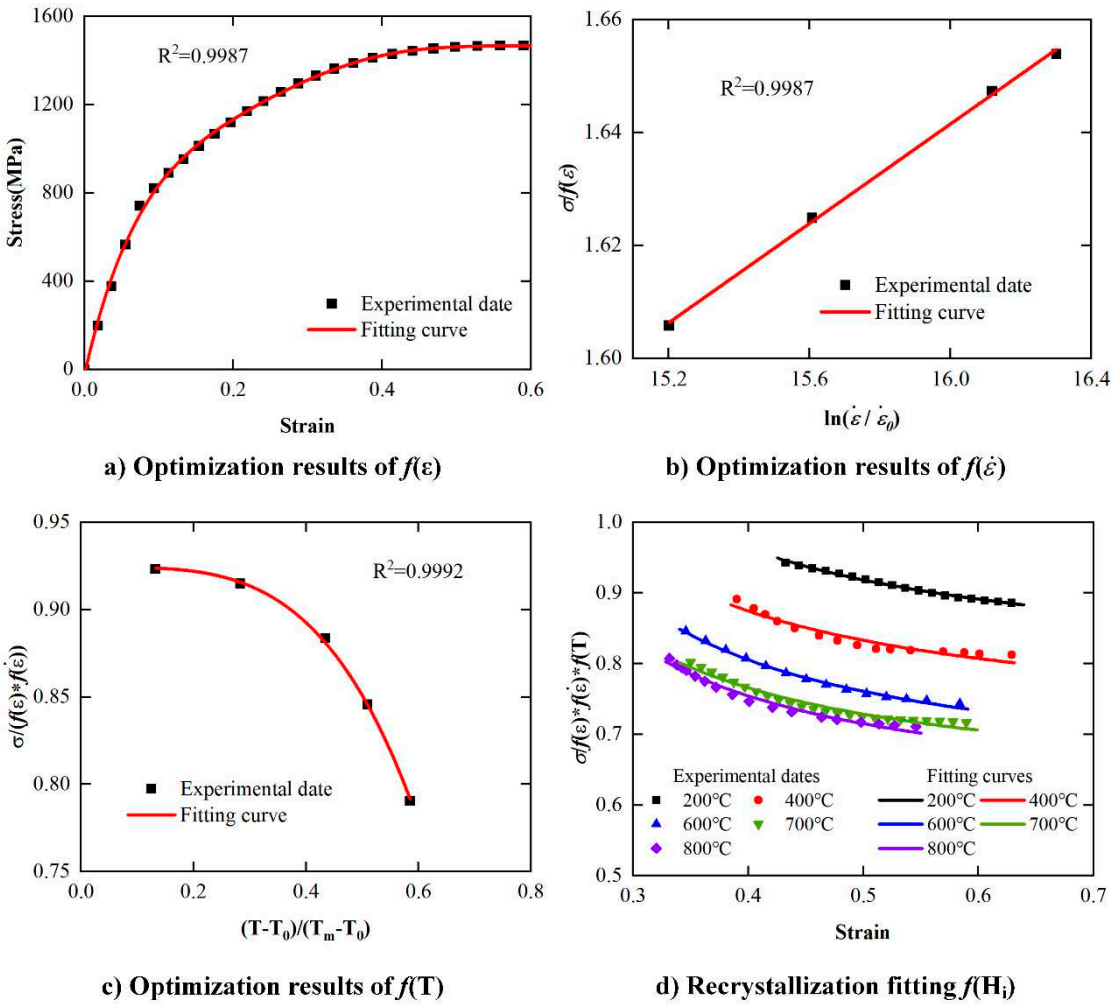

Figure 15. Function iteration method model solution results. a) Optimization results of $f(\varepsilon)$; b) Optimization results of $f(\dot{\varepsilon})$; c) Optimization results of f(T); d) Recrystallization fitting f(H_i).

Finally, the constitutive model constructed by the function iteration method is obtained, which is shown in Equation (24).

Preprints (www.preprints.org) | NOT PEER-REVIEWED | Posted: 7 December 2023 doi:10.20944/preprints202312.0453.v1

$$\sigma = (427.05 + 4856.82\varepsilon - 7502.10\varepsilon^2 + 4053.41\varepsilon^3 - 381.92\varepsilon^4) \times (0.969 + 0.042ln(\frac{\dot{\varepsilon}}{\dot{\varepsilon}_0})) \times (0.924 - (\frac{T - T_0}{T_m - T_0})^{3.768}) \times \left[(1 - (-0.008 / \varepsilon + 7.094) + (-0.008 / \varepsilon + 0.479) \ln(\frac{\dot{\varepsilon}}{\dot{\varepsilon}_0}) \right]^{-1} \quad (24)$$

(3) Comparison of different methods

In order to optimize the solution method of the parameters, the stress-strain curves obtained by the constitutive equations solving by the two methods described in the previous section are compared with the experimental results. Under the condition of strain rate is 10000s^{-1} and the temperature is 25℃, 200℃, 400℃, 600℃, 700℃, 800℃, the comparison results of stress-strain curves are shown in Figure 16. Figure 16a,b are the experimental comparison results of linear regression solving method and functional iteration solving method, respectively. According to Figure 16, both of the equations obtained by linear regression solving method and functional iteration solving method can predict the trend of flow stress.

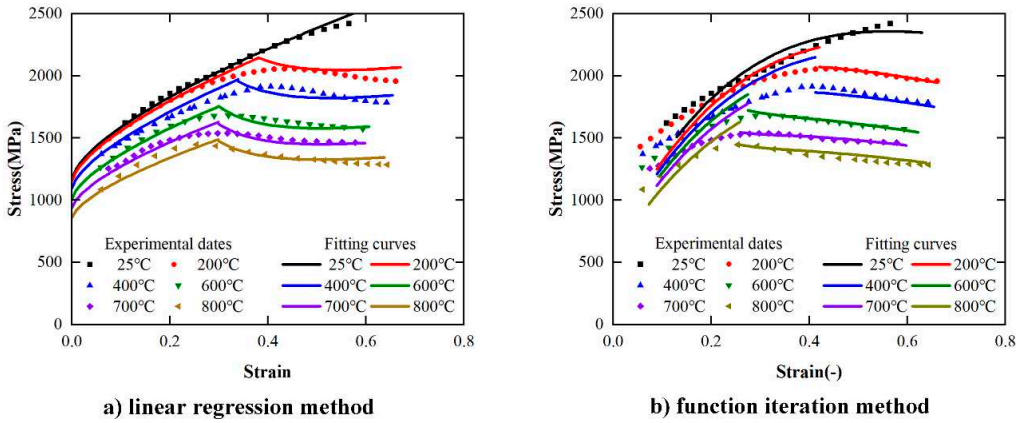

Figure 16. Comparison of experimental results and predicted results ($\dot{\varepsilon} = 10000s^{-1}$). a) Linear regression method; b) Function iteration method.

In order to quantitatively evaluate the overall error of the two methods, the scatter plot is used to calculate the correlation value. The results of the correlation between the calculated stress and the experimental stress obtained by the two methods are shown in Figure 17. Figure 17a,b are the results of linear regression solving method and functional iteration solving method, respectively. Compared with Figure 17b (R^2 = 0.889), the data correlation index in Figure 17a is higher (R^2 = 0.985), that is, the data concentration is higher.

Preprints (www.preprints.org) | NOT PEER-REVIEWED | Posted: 7 December 2023 doi:10.20944/preprints202312.0453.v1

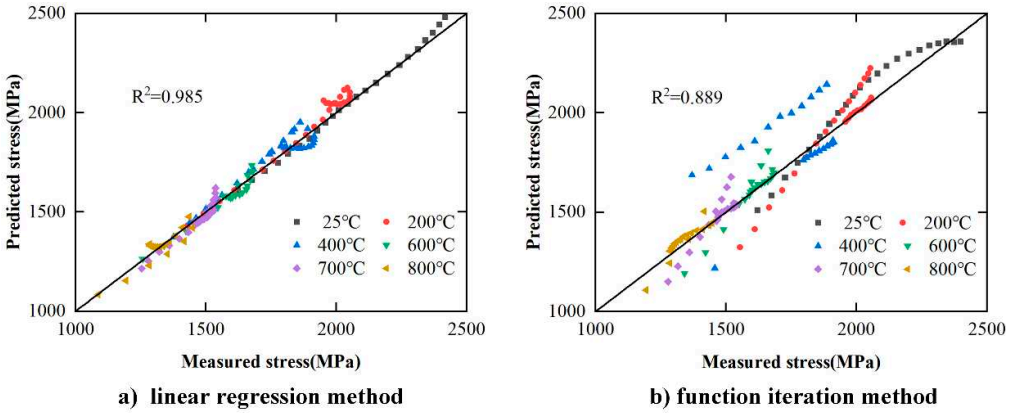

Figure 17. Comparison of correlation between predicted stress and measured stress by different solving methods. a) Linear regression method; b) Function iteration method.

The maximum relative error θ between the measured stress and the predicted stress is also calculated to evaluate prediction accuracy, as shown in Equation (25).

$$\theta = \max\left(\frac{|\sigma_p - \sigma_m|}{\sigma_m} \times 100\%\right) \tag{25}$$

Where, σ_p is the predicted stress, σ_m is the measured stress. The maximum relative error of the constitutive model obtained by the linear fitting method and the function iteration method are shown in Table 7. According to Table 7, the accuracy of the model obtained by the linear regression method (11.21%) is much higher than that obtained by the function iteration method (4.74%) in the non-dynamic recrystallization stage. Correspondingly, in the recrystallization stage, the accuracy of the model obtained by the function iteration method is improved (4.11%), which is very small compared with the accuracy of the model obtained by the linear regression method (5.11%). By calculating the average value of the maximum error $\overline{\theta}$ before and after dynamic recrystallization, the model accuracy obtained by the linear regression method is greater than the model obtained by the functional regression method.

Table 7. Comparison of the maximum relative errors of two different methods.

Maximum relative errors	Linear regression method	Function iteration method
$\theta_1(\varepsilon < \varepsilon_r)$	4.74%	11.21%
$\theta_2(\varepsilon \geq \varepsilon_r)$	5.11%	4.11%
$\overline{\theta}$	4.93%	7.66%

In summary, the J-C constitutive equation of PM superalloy proposed in this paper solved by linear regression method is shown in Equation (26).

$$\sigma = (773 + 1271\varepsilon^{0.667}) \times (1 + 0.031 ln(\frac{\dot{\varepsilon}}{\dot{\varepsilon}_0})) \times \left(1 - (\frac{T - T_0}{T_m - T_0})^{1.66 + 8.05 \times 10^{-5}\dot{\varepsilon}}\right) \times \left[(1 - (-0.015/\varepsilon - 0.015) + (-0.015/\varepsilon + 0.046)\ln(\frac{\dot{\varepsilon}}{\dot{\varepsilon}_0})\right]^{-1} \tag{26}$$

4.3. Validation of modified J-C constitutive model

Preprints (www.preprints.org) | NOT PEER-REVIEWED | Posted: 7 December 2023 doi:10.20944/preprints202312.0453.v1

Temperature-dependent J-C model [28,29] is also widely used to predict the flow stress behavior of materials in cutting process, which is shown in Equation (27).

$$\sigma = (A + B\varepsilon^{n})(1 + C\ln\frac{\dot{\varepsilon}}{\dot{\varepsilon}_0})\left[1 - \left(\frac{T - T_0}{T_m - T_0}\right)^{m}\right]\left(\frac{1}{1-(a-b\varepsilon)}\right) \quad (27)$$

Where, a, b are the coefficients related to flow softening caused by dynamic recrystallization. According to the stress-strain data of the PM superalloy under the experimental conditions in this paper, the linear regression method is used to solve Equation (24), and the established constitutive model is shown in Equation (28).

$$\sigma = (773 + 1271\varepsilon^{0.667})(1 + 0.031\ln\frac{\dot{\varepsilon}}{\dot{\varepsilon}_0})\left(1 - \left(\frac{T - T_0}{T_m - T_0}\right)^{1.66+8.05\times10^{-5}\dot{\varepsilon}}\right)\left(\frac{1}{1-(0.274-1.234\varepsilon)}\right) \quad (28)$$

The comparison between the predicted stress and the experimental stress of the two modified models at 10000s^{-1} strain rate are shown in Figure 18. Figure 18a,b are the comparison results of the model proposed in this paper and the Temperature-dependent J-C model, respectively.

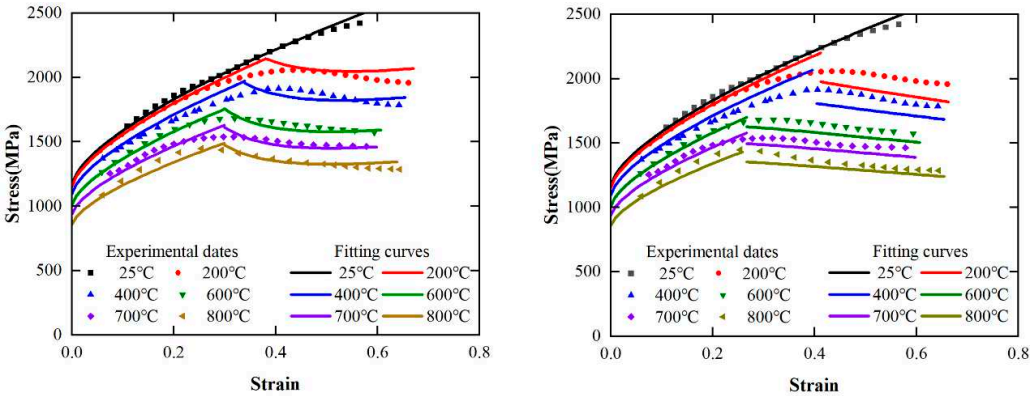

a) The modified J-C model proposed in this paper

b) Temperature-dependent J-C model

Figure 18. Comparison of correlation between predicted stress and measured stress by two models. (a) The modified J-C model proposed in this paper; (b) Temperature-dependent J-C model.

The results of the correlation analysis between the calculated stress and the experimental stress obtained by the two models are shown in Figure 19. Figure 19a,b are the correlation analysis results of model proposed in this paper and Temperature-dependent J-C model, respectively. Compared with Figure 19b (R^2=0.956), the data correlation index in Figure 19a is higher (R^2=0.985), that is, the data concentration is higher.

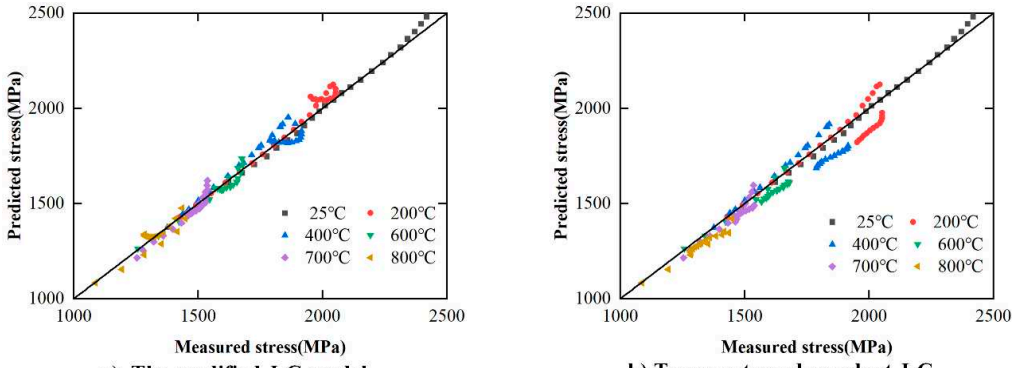

a) The modified J-C model proposed in this paper

b) Temperature-dependent J-C model

 doi:10.20944/preprints202312.0453.v1

Figure 19. Comparison of correlation between predicted stress and measured stress by different modified models. (a) The modified J-C model proposed in this paper; (b) Temperature-dependent J-C model.

According to Equation (25), the average values of the maximum relative error of the two models were calculated. The average value of the maximum relative errors of flow stress predicted by the modified J-C model in this paper and Temperature-dependent J-C model are 5.11% and 8.14%, respectively. Therefore, the constitutive model proposed in this paper can predict the flow stress of PM superalloy under the influence of recrystallization softening more accurately.

5. Conclusion

In this works, the dynamic mechanical properties of Nickel based PM superalloy are analyzed by quasi-static compression test and SHPB test at strain rate of $4000s^{-1}$ ~ $12000s^{-1}$ and temperature of 25°C ~ 800°C. A J-C constitutive model considering dynamic recrystallization softening effect is proposed. The following conclusions can be drawn in this paper.

(1) Dynamic mechanical properties of Nickel based PM superalloy was obtained by experiments. The PM superalloy has obvious plasticizing effect in the deformation process over a wide range of strain rate. The PM superalloy material exhibits a significant strain rate hardening effect and temperature softening effect. During the compression test, the strain hardening phenomenon of PM superalloy is significant and the strain hardening effect gradually weakens with the continuous increase of strain. FGH96 superalloy exhibits weak strain rate sensitivity and strong temperature sensitivity.

(2) Considering the influence of temperature and strain rate, the formula for the flow stress softening term $H(\varepsilon,\dot{\varepsilon},T)$ and critical strain ε_r of dynamic recrystallization were obtained. On this basis, the modified J-C constitutive model of PM superalloy considering dynamic recrystallization behavior in a wide range of strain rate and temperature is proposed.

(3) The coefficients of the modified constitutive equation established in this paper were obtained by linear fitting and function iteration respectively. Through correlation analysis and maximum error analysis, the modified constitutive equation solved by the linear fitting method has higher accuracy.

(4) Compared with the temperature-dependent constitutive model, it is found that the modified constitutive model established in this paper is more suitable for the description of the stress-strain relationship of PM superalloy at high temperature and high strain rate.

Data Availability Statement: In this section, please provide details regarding where data supporting reported results can be found, including links to publicly archived datasets analyzed or generated during the study. Please refer to suggested Data Availability Statements in section "MDPI Research Data Policies" at https://www.mdpi.com/ethics. You might choose to exclude this statement if the study did not report any data.

Acknowledgments: The project is supported by National Natural Science Foundation of China (No. 52105460). This work is also supported by grants from China Postdoctoral Science Foundation (2022M71190), Shandong Provincial Key Research and Development Program (Major Scientific and Technological Innovation Project) (No.2020CXGC010204), Natural Science Foundation of Shandong Province (ZR202111150191), Key Laboratory of High-efficiency and Clean Mechanical Manufacture at Shandong University and Taishan Scholar Foundation.

Conflicts of Interest: The authors declare no conflict of interest.

References

1. Boyer R, Cotton J, Mohaghegh M, Schafrik R J M B. Materials considerations for aerospace applications[J]. 2015, 40(12): 1055-1066. https://doi.org/10.1557/mrs.2015.278
2. Yang L, Ren X, Ge C, Yan Q J I J o M R. Status and development of powder metallurgy nickel-based disk superalloys[J]. 2019, 110(10): 901-910. https://doi.org/10.3139/146.111820.
3. Yang L, Ren X, Ge C, Yan Q. Status and development of powder metallurgy nickel-based disk superalloys[J]. International Journal of Materials Research, 2019, 110(10): 901-910. https://doi.org/10.3139/146.111820

4. Selvaraj S K, Sundaramali G, Jithin Dev S, et al. Recent Advancements in the Field of Ni-Based Superalloys[J]. Advances in Materials Science and Engineering, 2021, 2021: 1-60. https://doi.org/10.1155/2021/9723450
5. Zhang X, Chen Y, Hu J. Recent advances in the development of aerospace materials[J]. Progress in Aerospace Sciences, 2018, 97: 22-34. https://doi.org/10.1016/j.paerosci.2018.01.001
6. Guo N, Leu M C. Additive manufacturing: technology, applications and research needs[J]. Frontiers of mechanical engineering, 2013, 8: 215-243. https://doi.org/10.1007/s11465-013-0248-8
7. Zhang H, Zeng H, Yan R, Wang W, Peng F J T I J o A M T. Analytical modeling of cutting forces considering material softening effect in laser-assisted milling of AerMet100 steel[J]. 2021, 113: 247-260. https://doi.org/10.1007/s00170-020-06518-w
8. Melkote S N, Grzesik W, Outeiro J, et al. Advances in material and friction data for modelling of metal machining[J]. 2017, 66(2): 731-754. https://doi.org/10.1016/j.cirp.2017.05.002
9. Ucun İ, Aslantas K J T I J o A M T. Numerical simulation of orthogonal machining process using multilayer and single-layer coated tools[J]. 2011, 54: 899-910. https://doi.org/10.1007/s00170-010-3012-9
10. Hou X, Liu Z, Wang B, et al. Stress-strain curves and modified material constitutive model for Ti-6Al-4V over the wide ranges of strain rate and temperature[J]. Materials, 2018, 11(6): 938. https://doi.org/10.3390/ma11060938
11. Liu H, Xu X, Zhang J, et al. The state-of-the-art on numerical simulation of the effect of microstructure and its evolution in metal cutting processes[J]. International Journal of Machine Tools and Manufacture, 2022: 103890. https://doi.org/10.1016/j.ijmachtools.2022.103890
12. Johnson G R. A constitutive model and data for materials subjected to large strains, high strain rates, and high temperatures[J]. Proc 7th Inf Sympo Ballistics, 1983: 541-547.
13. He A, Xie G, Zhang H, Wang X. A comparative study on Johnson–Cook, modified Johnson–Cook and Arrhenius-type constitutive models to predict the high temperature flow stress in 20CrMo alloy steel[J]. Materials & Design (1980-2015), 2013, 52: 677-685. https://doi.org/10.1016/j.matdes.2013.06.010
14. Shokry A, Gowid S, Mulki H, Kharmanda G. On the Prediction of the Flow Behavior of Metals and Alloys at a Wide Range of Temperatures and Strain Rates Using Johnson–Cook and Modified Johnson–Cook-Based Models: A Review[J]. Materials, 2023, 16(4): 1574. https://doi.org/10.3390/ma16041574
15. Su X, Wang G, Li J, Rong Y J S. Dynamic mechanical response and a constitutive model of Fe-based high temperature alloy at high temperatures and strain rates[J]. 2016, 5(1): 1-14. https://doi.org/10.1186/s40064-016-2169-6
16. Sakai T, Belyakov A, Kaibyshev R, Miura H, Jonas J J. Dynamic and post-dynamic recrystallization under hot, cold and severe plastic deformation conditions[J]. Progress in materials science, 2014, 60: 130-207. https://doi.org/10.1016/j.pmatsci.2013.09.002
17. Shin H, Ju Y, Choi M K, Ha D H. Flow stress description characteristics of some constitutive models at wide strain rates and temperatures[J]. Technologies, 2022, 10(2): 52. https://doi.org/10.3390/technologies10020052
18. Calamaz M, Coupard D, Girot F J I J o M T, Manufacture. A new material model for 2D numerical simulation of serrated chip formation when machining titanium alloy Ti–6Al–4V[J]. 2008, 48(3-4): 275-288.https://doi.org/10.1016/j.ijmachtools.2007.10.014
19. Ulutan D, Sima M, Özel T J A M R. Prediction of machining induced surface integrity using elastic-viscoplastic simulations and temperature-dependent flow softening material models in titanium and nickel-based alloys[J]. 2011, 223: 401-410. https://doi.org/10.4028/www.scientific.net/AMR.223.401
20. Rotella G, Umbrello D. Finite element modeling of microstructural changes in dry and cryogenic cutting of Ti6Al4V alloy[J]. Cirp Annals, 2014, 63(1): 69-72. https://doi.org/10.1016/j.cirp.2014.03.074
21. Liang X, Liu Z, Wang B, Hou X J I J o M S. Modeling of plastic deformation induced by thermo-mechanical stresses considering tool flank wear in high-speed machining Ti-6Al-4V[J]. 2018, 140: 1-12. https://doi.org/10.1016/j.ijmecsci.2018.02.031
22. Denguir L, Outeiro J, Fromentin G, Vignal V, Besnard R J J o M P T. A physical-based constitutive model for surface integrity prediction in machining of OFHC copper[J]. 2017, 248: 143-160. https://doi.org/10.1016/j.jmatprotec.2017.05.009Get rights and content
23. Pan Z, Wu Z, Xiong J J P T. High-speed infrared imaging and mesostructural analysis of localized temperature rise in damage and failure behavior of 3-D braided carbon/epoxy composite subjected to high strain-rate compression[J]. 2019, 80: 106151. https://doi.org/10.1016/j.polymertesting.2019.106151

24. Liang H, Guo H, Nan Y, et al. The construction of constitutive model and identification of dynamic softening mechanism of high-temperature deformation of Ti–5Al–5Mo–5V–1Cr–1Fe alloy[J]. 2014, 615: 42-50. https://doi.org/10.1016/j.msea.2014.07.050
25. Guo Y, Ruan Q, Zhu S, et al. Temperature rise associated with adiabatic shear band: causality clarified[J]. 2019, 122(1): 015503. https://doi.org/10.1016/j.msea.2014.07.050
26. Su X, Wang G, Li J, Rong Y J S. Dynamic mechanical response and a constitutive model of Fe-based high temperature alloy at high temperatures and strain rates[J]. 2016, 5(1): 1-14. https://doi.org/10.1186/s40064-016-2169-6
27. Lin Y, Chen X-M, Liu G J M S, A E. A modified Johnson–Cook model for tensile behaviors of typical high-strength alloy steel[J]. 2010, 527(26): 6980-6986. https://doi.org/10.1016/j.msea.2010.07.061
28. Murugesan M, Jung D W J M. Johnson Cook material and failure model parameters estimation of AISI-1045 medium carbon steel for metal forming applications[J]. 2019, 12(4): 609. https://doi.org/10.3390/ma12040609
29. Andrade U, Meyers M, Vecchio K, Chokshi A H J A m e m. Dynamic recrystallization in high-strain, high-strain-rate plastic deformation of copper[J]. 1994, 42(9): 3183-3195. https://doi.org/10.1016/0956-7151(94)90417-0
30. Ashrafian M M, Hosseini Kordkheili S A J P o t I o M E, Part G: Journal of Aerospace Engineering. A novel phenomenological constitutive model for Ti-6Al-4V at high temperature conditions and quasi-static strain rates[J]. 2021, 235(13): 1831-1842. https://doi.org/10.1177/0954410020985990